Nanoscale

COMMUNICATION

View Article Online
View Journal | View Issue

Cite this: *Nanoscale*, 2023, **15**, 9297

Received 20th February 2023,
Accepted 2nd May 2023

DOI: 10.1039/d3nr00808h

rsc.li/nanoscale

Laser doping of 2D material for precise energy band design†

Xiang Tan,‡[a,b] Shu Wang,‡[a] Qiaoxuan Zhang,‡[c] Juxing He,[a] Shengyao Chen,[a,e] Yusong Qu,[a] Zhenzhou Liu,[a,f] Yong Tang,[c] Xintong Liu,[c] Cong Wang,*[d] Quan Wang *[b] and Qian Liu *[a,e]

The number of excellent 2D materials is finite for nano optoelectric devices including transistors, diodes, sensors, and so forth, thus the modulation of 2D materials is important to improve the performance of the current eligible 2D materials, and even to transform unqualified 2D materials into eligible 2D materials. Here we develop a fine laser doping strategy based on highly controllable laser direct writing, and investigate its effectivity and practicability by doping multilayer molybdenum ditelluride ($MoTe_2$). Power-gradient laser doping and patterned laser doping, for the first time, are presented for designable and fine doping of 2D materials. The laser-induced polar transition of $MoTe_2$ indicates good controllability of the method for the carrier concentration distribution in $MoTe_2$. Multiple devices with finely tuned energy band structures are demonstrated by means of power-gradient laser doping and patterned laser doping, further illustrating the design capability of a precise energy band in 2D materials.

1. Introduction

Fast-developing information technologies such as big data, internet of things, *etc.*, expect faster computing speed and lower power consumption,[1] resulting in a further decrease in transistor channel in length and thickness. But when the channel is reduced to a few nanometres, a significant increase in surface and internal defects in transistors will hinder the movement of electrons and reduce the gate capacitance, thus causing a low carrier mobility and large gate voltage.[2] Although these can be improved by different structures using double gates, nanowire gates, and fin gates, the carrier mobility and gate voltage are still limited due to the defects. As a result, the channel width, so far, cannot break through 5 nm.[3] The new-type materials adopted might be an efficient solution. As emerging materials, two-dimensional materials (2D materials) with atomic thin layer thicknesses less than 1 nm can greatly reduce surface and interface defects, enhance carrier mobility, and decrease power consumption, due to their high crystal quality and superthin thickness. Therefore, 2D materials have great potential as promising materials for use for nano optoelectric devices including transistors, diodes, sensors, and so forth.[4] However, the number of excellent 2D materials suitable for applications remains finite, thus modulation of 2D materials is important to improve performance of the current eligible 2D materials, and even to transform unqualified 2D materials into eligible 2D materials.

Doping, as an important means of modulating semiconductor materials and devices, is a critical issue in almost all semiconductor fabrication. At present, thermal diffusion doping and ion implantation doping are widely used in industries to modulate the properties of traditional semiconductor devices.[5] However, for 2D materials, these mature doping strategies will lead to lattice distortion and unfavorable defects,[6] which might not be fully compatible with 2D materials. In recent years, studies have shown that plasma, chemical reaction, and heating can also induce doping in 2D materials,[7] but these doping methods realize designable and local modulation in 2D materials with difficulty, and some might even induce annoying contamination. Photothermal doping, as a newly developed method, is a pollution-free method and can complete doping in the desired area. For 2D materials, the photothermal effect will merge the O_2 and H_2O in the atmosphere

[a]*CAS Center for Excellence in Nanoscience, National Center for Nanoscience and Technology & University of Chinese Academy of Sciences, Beijing 100190, China. E-mail: liuq@nanoctr.cn, wangcongphysics@mail.buct.edu.cn, wangq@ujs.edu.cn*
[b]*Zhenjiang key laboratory of advanced sensing materials and devices, Jiangsu University, Zhenjiang 212013, PR China*
[c]*Hebei University of Water Resources and Electric Engineering Electrical Automation Department, 061001 Cangzhou, Hebei, China*
[d]*College of Mathematics and Physics, Beijing University of Chemical Technology, Beijing, 100029, China*
[e]*MOE Key Laboratory of Weak-Light Nonlinear Photonics, TEDA Applied Physics Institute, School of Physics, Nankai University, Tianjin 300457, China*
[f]*School of Physical Science and Technology, Inner Mongolia University, Inner Mongolia 010000, China*

†Electronic supplementary information (ESI) available. See DOI: https://doi.org/10.1039/d3nr00808h

‡These authors contributed equality to this work

into the material,[8] which is quite similar to heating in the atmosphere.[9] Based on this route, it is possible to control the hole carrier concentration and even the polarity shift in 2D materials to develop high-performance junctions, memory, low-contact barriers, and logic devices.[10]

The laser direct writing (LDW) technique has gathered plenty of attention and made great progress because of its flexibility and compatibility in nano–micro fabrication.[11] LDW not only ensures high precision, but also has the advantages of low cost and low practical operation difficulty with electron beam doping. More importantly, LDW can be photothermally doped according to the designed pattern, and can remove the pollutants attached to the surface. Therefore, LDW provides a feasible tool to perform ultrafine photothermal doping on 2D materials.[12] At the same time, it is critical for 2D-material-based electronics[13] to explore the LDW doping of 2D materials, including the doping features and mechanism, and detailed composition variation in ultrafine doping.

In this work, a modified LDW system with super-resolution fabrication ability is adopted to perform ultrafine photothermal doping. Here, taking $MoTe_2$ as an example, ultrafine laser doping has been deeply investigated with regard to modulation controllability, doping features, and mechanism. The results show that the local p-doping level in $MoTe_2$ can be well controlled by modulating laser parameters such as laser power, irradiation time, *etc*. Moreover, for the first time, we present power gradient laser doping and patterned laser doping of 2D materials. The corresponding ultrafine tuning of the carrier distribution and energy band structure is also clarified through simulation and calculation. Owing to the simplicity and flexibility of our LDW doping method, it will provide a powerful means for ultrafine photothermal doping, and will open many new application opportunities for 2D-material-based nanoelectronics.

2. Experimental

A super-resolution laser direct writing system (HWN LDW-L4) has been adopted for conducting photothermal doping. The laser wavelength is 405 nm with a laser spot diameter of approximately 300 nm. Multilayer $MoTe_2$ is mechanically exfoliated from bulk 2H-$MoTe_2$ crystals using tap (NITTO, 224S) and polydimethylsiloxane (Gel-Pak, PF). The crystal structure of multilayer $MoTe_2$ was characterized by transmission electron microscopy (TEM, JEM-2100). During doping, the laser pulse width was set at 2000 ns, the spatial scanning step length was 100 nm, and the laser power varied from 0 mW to 25.8 mW. The surface morphology of the $MoTe_2$ after laser action was characterized using optical microscopy (Olympus, LEXT-OLS4000) and scanning electron microscopy (SEM, Hitachi-SU8220), and the elemental variation of Mo and Te was analyzed using X-ray energy dispersive spectrometry (EDS, Hitachi-SU8220). $MoTe_2$ processed under different laser powers was characterized using a Raman spectrometer (Renishaw, inVia Plus). The thickness and surface potential changes of the $MoTe_2$ were measured using atomic/Kelvin-probe force microscopy (AFM/KPFM, Multimode 8HR).

The Au (25 nm)–Cr (5 nm) bottom electrode was prepared on SiO_2 (300 nm)/Si substrate by magnetron sputtering (Kurt J. Lesker PVD 75) for the 2D-material devices. The multilayer $MoTe_2$ was mechanically transferred onto the electrodes and then photothermally doped using LDW. Heat transfer simulation of laser treatment was performed using "COMSOL Multiphysics Software", and modelling and parameters were referenced from experiments. The electrical measurements of the devices were performed using a four-probe electrical test system with a three-channel sourcemeter (Keithley 2635 and 2602). Density functional theory (DFT) was performed using the Vienna *ab initio* Simulation Package (VASP).

3. Results and discussion

3.1 Characterization of laser-irradiated $MoTe_2$

To systematically analyze the photothermal doping effect on $MoTe_2$, a 25-layer 2H-$MoTe_2$ (approximately 15 nm, the number of layers of the sample was roughly determined by an optical microscope), whose crystal quality and thickness had been verified by TEM and AFM (Fig. S1 and S2†),[14] was transferred onto a SiO_2 wafer and irradiated using a laser under the atmosphere. The laser, with power ranging from 0 mW to 25.8 mW and a pulse width of 2000 ns, scanned from right to left (Fig. S3†). An obvious change in morphology of the $MoTe_2$ can be observed after the laser doping in the SEM image, as shown in Fig. 1a. The results indicate that the doping effect is

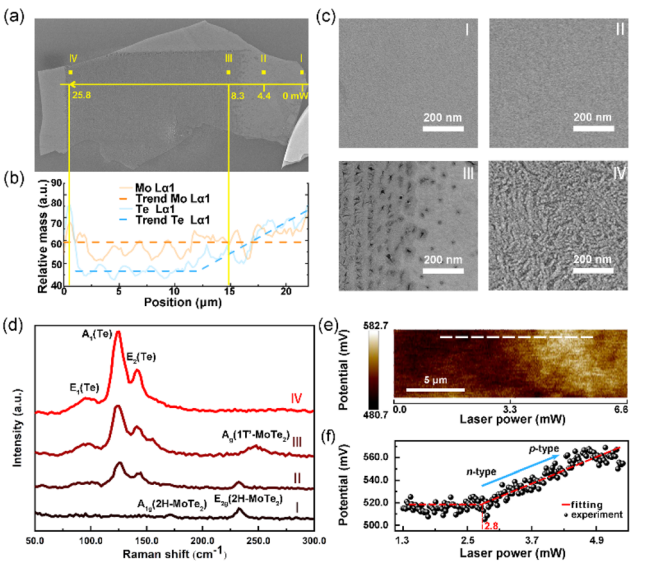

Fig. 1 Device fabrication and characterization of $MoTe_2$ after laser irradiation. (a) Schematic picture of the device. (b) EDS analysis of the $MoTe_2$ along the yellow line in (a) after laser scanning of the area. (c) SEM image of $MoTe_2$ irradiated under four typical powers: I, 0 mW; II, 4.4 mW; III, 8.3 mW; and IV, 25.8 mW. (d) Raman spectrum of $MoTe_2$ at I, II, III and IV after laser treatment in figure (c). (e and f) The surface potential of the $MoTe_2$ after laser irradiation from 0 to 6.6 mW is measured by KPFM, which can reflect the variation of the Fermi level.

stronger with increasing laser power, but when the power is over 8.3 mW, the material structure starts to be destroyed accompanied by holes and clusters appearing on the surface. The thickness of the $MoTe_2$ does not change obviously with laser power less than 8.3 mW, while the $MoTe_2$ surface becomes obviously rough for power higher than 8.3 mW, as shown in Fig. 1a.

To understand composition variations of $MoTe_2$ after laser action at different powers, EDS analysis along the horizontal yellow line in Fig. 1a was performed, as shown in Fig. 1b. The Te elemental mass (blue curve) gradually decreases with increasing laser power and tends toward a stable value, while the Mo elemental mass (orange curve) is almost constant. The decrease in Te atoms should be attributed to the adsorption of O_2 and H_2O due to an increase in thermal motion of the Te atoms under laser action, and eventually leads to Te vacancy defects. The four typical morphologies of the 2H-$MoTe_2$ (I, 0 mW; II, 4.4 mW; III, 8.3 mW; IV, 25.8 mW) are shown in Fig. 1c. Moreover, the Raman spectra (Fig. 1d and Fig. S4a†) show 1T′-$MoTe_2$, 2H-$MoTe_2$ and Te for different powers. When the laser power gradually increases from I to II, the intensities of two characteristic peaks of 2H-$MoTe_2$ at 171 cm^{-1} and 232 cm^{-1} gradually weaken, indicating the entrance of foreign molecules. Te peaks also begin to appear at this stage at 90 cm^{-1}, 123 cm^{-1}, and 141 cm^{-1}, corresponding to the E_1, A_1, and E_2 modes.[15] Due to the high atomic number and large electron polarization rate of Te, the peaks of Te are more prominent, leading to the signal of the A_{1g} peak of 2H-$MoTe_2$ disappearing. From II to III, holes (Fig. 1cIII) started to be generated on the surface of the $MoTe_2$, the E_{2g} peak of 2H-$MoTe_2$ disappeared, and the A_g peak of 1T′-$MoTe_2$ appeared at 248 cm^{-1}, indicating that a phase transition occurred in the $MoTe_2$ and the intensity of the Te peak increased. As the laser power further increased (from III to IV), the $MoTe_2$ surface was damaged severely (Fig. 1cIV), the A_g peak of 1T′-$MoTe_2$ gradually weakened and eventually disappeared, and only the Te peak remained. The peak intensity variation (Fig. S4b†) was calculated through the Raman results, which indicated that the 2H-$MoTe_2$ was transformed into 1T′-$MoTe_2$ under a low-power laser, and the 1T′ structure was destroyed when the power was over 8.3 mW, while Te gradually precipitated and eventually formed a Te cluster on the $MoTe_2$ surface.

These results present changes in morphology and elements of the $MoTe_2$ under laser irradiation. The destruction of the material is unfavorable in doping, thus the doping power used for laser doping is set beneath the threshold of the phase change (4.4 mW). The surface potential of the $MoTe_2$ after laser irradiation from 0 to 6.6 mW was measured by KPFM, which can reflect the variation of the Fermi level as shown in Fig. 1e and f. The surface potential at the irradiated region firstly remains steady and then increases with increasing laser power. When the laser power is between 2.8 mW and 4.4 mW, the surface potential increases (the Fermi surface moves downward) linearly with the laser power.[10] The result proves the ability of laser doping to finely control the Fermi level and the doping level. Based on this effect, planar $MoTe_2$ devices with various types of ultrafine doping modes were designed and tested to verify their applicability in complex electronic circuits.

3.2 Electrical transport properties of photothermal doped $MoTe_2$

Fig. 2a schematically describes the fabrication process of the device (details see Fig. S5†). A simple verification experiment on the resistance measurement of the device further identified the laser doping validity (Fig. S6†), encouraging further investigation of the electrical transport properties. As shown in Fig. 2b, the electrical measurements indicate that the mechanically exfoliated pristine $MoTe_2$ in the device shows n-type characteristics ($MoTe_2$ is partially transformed to n-type when it is larger than 5 layers),[16] while $MoTe_2$ appears bipolar after the laser action of 3.0 mW and completely transforms into a p-type semiconductor with a switching ratio of 104 under the laser action of 4.4 mW. It should be stressed that for p-doping, the temperature induced by the laser is important and thus the temperature distribution in this case was simulated, where the highest temperature was around 500 K (Fig. 2c).

To reveal the mechanism of the polarity shift of the $MoTe_2$ induced by laser doping, energy band calculations of different doping situations were conducted, as shown in Fig. 2d–f. According to previous works, laser irradiation on $MoTe_2$ mainly involves two types of doping, vacancy doping and O_2 cluster doping.[10] Raman measurement further proves that the oxygen exists as clusters instead of MoO_3 or other compounds such as MoO_2 (Fig. S7†), indicating that O_2 was adsorbed into $MoTe_2$ and that no substitution doping of Te atoms occurred. Thus, we followed the characterization results and built the device model. To study the effect of the defect states, we took a 10 nm-length channel FET (with three layers of $MoTe_2$ and six layers of Au electrodes) as an example, and considered three cases (Fig. S8†): (i) no vacancies in the channel region; (ii) Te vacancies in all the three layers in the channel region; and (iii) Te vacancies and O_2 cluster absorption in the channel region. The total local density of states (LDOS) in each case is illustrated in Fig. 2d–f. Metal hybridization in the band gap of the pure Te defected case (ii) is obviously stronger in the channel region compared with the no defect case (i) and obviously lower than the O_2 cluster adsorption case (iii). Moreover, the position of the Fermi level relative to the valence band maximum in the channel is obviously lower in cases (ii) and (iii) compared with the original case (i). This is due to the Te vacancies and exposure to air of the $MoTe_2$ layers inducing hole (p-type) doping. According to the LDOS of the channel region from three layers of $MoTe_2$ FETs with Au electrodes, the effective SBH (0.24 eV) can be extracted (Fig. S9†). The simulation results are well consistent with the measurements and clearly demonstrate the mechanism of the doping effect, which enables us to perform more complicated and delicate tuning of $MoTe_2$.

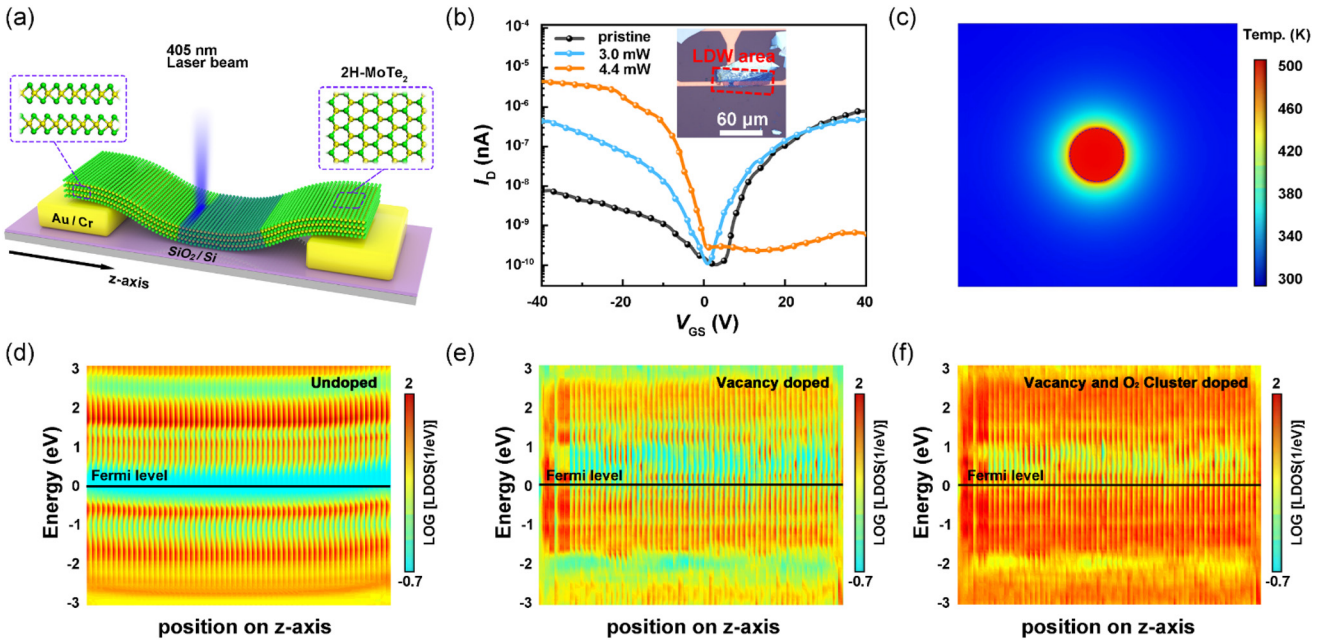

Fig. 2 Electrical behavior and mechanistic explanation of laser p-doped $MoTe_2$. (a) Schematic diagram of $MoTe_2$ irradiated by a laser. (b) Transfer curve of $MoTe_2$ after different power laser actions, where the illustration is the optical image of the device in the experiment. (c) Temperature distribution of $MoTe_2$ under laser irradiation, where the laser power is 4.4 mW and the pulse width is 2000 ns. (d–f) Total local density of states (LDOS) in the channel region of $MoTe_2$ under intrinsic and defect states. The channel length is 10 nm.

3.3 Laser modulation to energy band of $MoTe_2$

Generally, ultra-fine tuning of the band structure in 2D materials can be implemented by controlling laser parameters such as irradiation time, laser power, *etc*. But for a 2D-material-based device, the ultra-fine tuning effect will also depend on the laser-doping mode, doping shape and so on. For further exploring these fascinating features, four typical doping modes were designed and fabricated, as shown in Fig. 3.

In the first case where the laser irradiates the whole channel to produce doping (Fig. 3a), the energy band shifts upward, and the device conductivity is slightly enhanced due to the increased number of hole carriers, but no rectification is observed (Fig. 3b). However, when the laser irradiates the half channel rather than whole channel to produce doping (Fig. S10†), the *I*–*V* curves of the device show that the rectification ratio is sensitive to laser doping, and such strong rectification is a direct demonstration of the laser-induced pn junction.[10] In order to confirm the applicability of the laser-functionalized p-doping, the excellent electrical features in devices with integrated n–n, n–p, p–p, and n–p–n junctions (Fig. S11†) were further demonstrated. The rectification ratio of the $MoTe_2$ in-plane p–n junction prepared by laser doping is 102, which is much smaller than that of the traditional silicon-based p–n junction. In addition, laser doping in semiconductor materials can be designed in pattern because the LDW can controllably dope according to designed pattern. Laser doping of two-dimensional materials to prepare p–n junctions has the obvious advantages of no pollution, low cost, strong designability and universality.

For the second situation (Fig. 3c), the laser still irradiates the whole channel by adopting a gradient laser power to dope. This will result in the hole concentration distribution of the 2D $MoTe_2$ tending to be uphill and the energy band being warped, so that a unidirectional barrier is introduced. The device modulated using the method mentioned above exhibits a rectification effect and the switching ratio reaches 10^2 (Fig. 3d).

In the third and fourth situations, shape-dependent local laser dopings (rectangular and triangular) are carried out at the center of the device channel (Fig. 3e and g). Rectangular pattern doping forms a homogeneous junction with symmetric energy band bending of potentials across the channel, introducing a transverse potential barrier difference between the electrodes and thus lowering the conductivity, as shown in Fig. 3f. Triangular pattern doping forms a unidirectional potential barrier, leading the device to have a strong rectification effect with a switching ratio of 10^2 (Fig. 3h).

These experiments show that band structure in 2D material devices can be modulated flexibly by different laser doping modes. And some new features we obtained in the devices indicate that local and patterned laser doping as well as gradient-power laser doping are feasible and have great potential in the energy band modification of 2D materials.

To further verify the capacity of patterned laser doping and power-gradient laser doping, a triangular laser-doped junction was adopted for further experiments. As shown in Fig. 4a, the

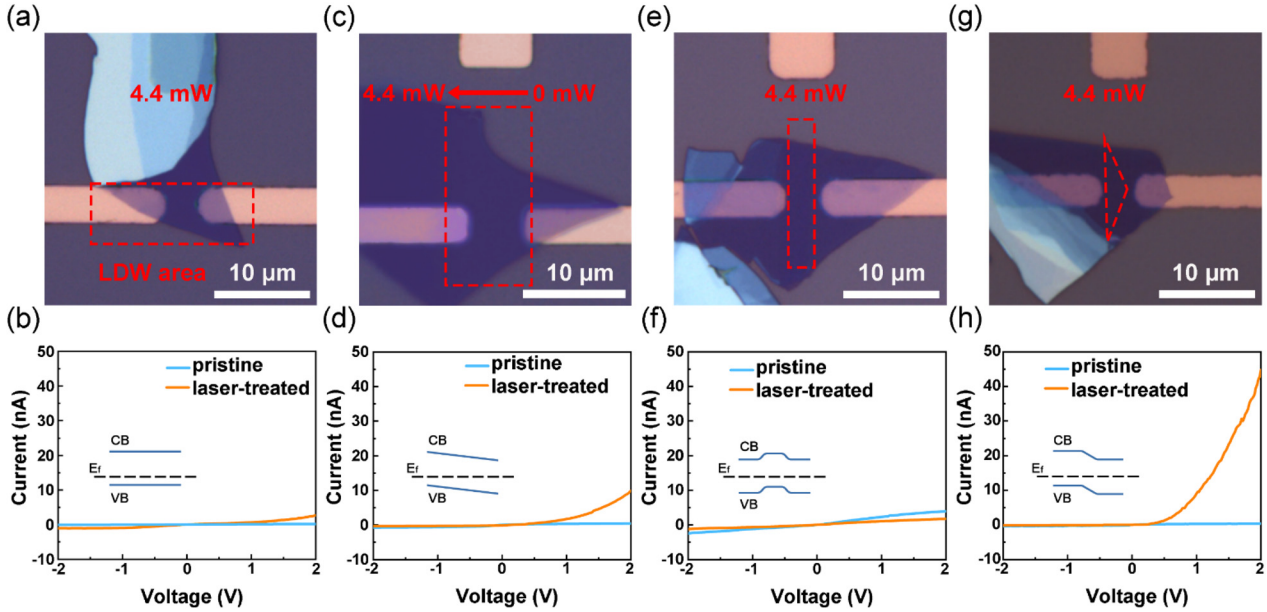

Fig. 3 Laser doping modulates the electrical properties and energy band distribution of $MoTe_2$. (a and b) Optical photographs and *I*–*V* characteristics of uniform power laser-doped $MoTe_2$, the inset in (b) is the corresponding band structure. The laser power is 4.4 mW and the laser pulse width is 2000 ns. (c and d) Optical photographs and *I*–*V* characteristics of $MoTe_2$ doped using the power gradient laser; the inset in (d) is the corresponding band structure. The laser power ranges from 4.4 mW to 0 mW, and the laser pulse width is 2000 ns. (e and f) Optical photographs and *I*–*V* characteristics of $MoTe_2$ doped with a rectangular symmetric pattern laser in the center of the channel; the inset in (f) is the corresponding band structure. The laser power is 4.4 mW and the laser pulse width is 2000 ns. (g and h) Optical photographs and *I*–*V* characteristics of $MoTe_2$ doped with a triangular pattern (area gradient) laser in the center of the channel; the inset in (h) is the corresponding band structure. The laser power is 4.4 mW and the laser pulse width is 2000 ns.

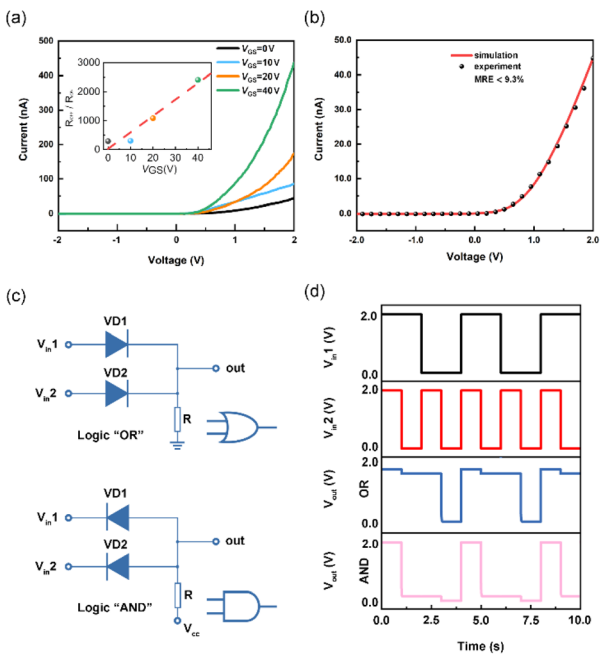

Fig. 4 Gate voltage regulation and logic gate circuit simulation of laser-doped $MoTe_2$. (a) *I*–*V* characteristics of triangular pattern laser-doped $MoTe_2$ at different gate pressures, where the inset shows the rectification ratio of the device at different gate voltages. (b) Diode model built from the characteristic parameters of $MoTe_2$ after laser doping of the triangular pattern. (c) Schematic diagram of a logic gate 'OR' and 'AND'. (d) Simulation results of the built logic gate circuit.

rectification ratio of the device can be regulated by the gate voltage, and the corresponding diode model is also constructed in a simulation program with integrated circuit emphasis (SPICE) based on the characteristic parameters of the device at $V_{gs} = 0$, with an average relative error MRE of less than 9.3%. Finally, the basic logic gates "OR" and "AND" (Fig. 4c) are built and verified using this model. The input and output of the logic gates show a steady performance (Fig. 4d), which further proves the applicability of the laser doping modulation. It should be stressed that there is often a large voltage drop when two-dimensional materials are applied to logic gate circuits. This means the performance of two-dimensional materials for electronic devices needs to be improved with regard to crystal quality and contact between electrodes and 2D materials, and so on.

4. Conclusions

A laser-doping method of 2D materials has been investigated deeply using a typical 2D-material $MoTe_2$. The realization of controlled p-type doping by a laser indicates the feasibility and effectivity of the laser doping, and the mechanism of the polarity transition of n-type $MoTe_2$ has also been revealed by applying energy band theory. Power-gradient laser doping and patterned laser doping are presented for the first time and their effectivity is also certified by the four typical energy band

modulations and the realization of an OR gate and an AND gate.

Compared with other 2D material doping techniques, the designability of laser doping is irreplaceable. Diverse and flexible laser-doping modes can be realized by modulating the laser power and laser irradiation time, and by gradient-power doping and shape-dependent doping. In principle, the laser doing method is suitable for any 2D materials, but the doping effect may be different for the same laser parameters and the same number of layers due to different crystal structures. It is believed that the laser fine-tuning method of 2D materials provides not only new ideas for the development of doping strategies but also many new application opportunities for 2D-material-based devices including resistors, memristors and diodes. In the future, capacitors and inductors will be realized by changing the target materials, laser parameters and laser direct writing methods, which is of significance for the development of future electronics.

Author contributions

Qian Liu, Cong Wang, and Quan Wang conceived and directed the study. Xiang Tan, Shu Wang, Juxing He, Shenyao Chen, Yusong Qu, carried out the investigations. Qiaoxuan Zhang, Yong Tang, and Xintong Liu implement simulation calculation. All authors participated in discussion of the results and wrote the manuscript.

Conflicts of interest

There are n conflicts to declare.

Acknowledgements

This work was supported by the National Natural Science Foundation of China (51971070, 10974037), the National Key Research and Development Program of China (2016YFA0200403), the CAS Strategy Pilot Program (XDA 09020300), and Eu-FP7 Project (No 247644).

References

1 (*a*) G. D. Spyropoulos, J. N. Gelinas and D. Khodagholy, *Sci. Adv.*, 2019, **5**, eaau7378; (*b*) A. I. Khan, A. Keshavarzi and S. Datta, *Nat. Electron.*, 2020, **3**, 588–597; (*c*) M. Si, Z. Lin, Z. Chen, X. Sun, H. Wang and P. D. Ye, *Nat. Electron.*, 2022, **5**, 164–170.

2 Y. Taur and T. H. Ning, *Fundamentals of Modern VLSI Devices*, Cambridge University Press, 2021.

3 (*a*) S.-K. Su, C.-P. Chuu, M.-Y. Li, C.-C. Cheng, H. S. P. Wong and L.-J. Li, *Small Struct.*, 2021, 2; (*b*) Q. Xie, J. Xu and Y. Taur, *IEEE Trans. Electron Devices*, 2012, **59**, 1569–1579; (*c*) I. Ferain, C. A. Colinge and J.-P. Colinge, *Nature*, 2011, **479**, 310–316; (*d*) Y. Zhai, Z. Feng, Y. Zhou and S.-T. Han, *Mater. Horiz.*, 2021, **8**, 1601–1617; (*e*) W. Ahmad, Y. Gong, G. Abbas, K. Khan, M. Khan, G. Ali, A. Shuja, A. K. Tareen, Q. Khan and D. Li, *Nanoscale*, 2021, **13**, 5162–5186.

4 (*a*) X.-L. Li, W.-P. Han, J.-B. Wu, X.-F. Qiao, J. Zhang and P.-H. Tan, *Adv. Funct. Mater.*, 2017, **27**, 1604468; (*b*) L. M. Xie, *Nanoscale*, 2015, **7**, 18392–18401; (*c*) S. Zeng, Z. Tang, C. Liu and P. Zhou, *Nano Res.*, 2021, **14**, 1752–1767.

5 (*a*) F. L. Bregolin, K. Krockert, S. Prucnal, L. Vines, R. Hübner, B. G. Svensson, K. Wiesenhütter, H.-J. Möller and W. Skorupa, *J. Appl. Phys.*, 2014, **115**, 064505; (*b*) A. Fave, J.-F. Lelièvre, T. Gallet, Q. Su and M. Lemiti, *Energy Procedia*, 2017, **124**, 577–583.

6 S. Behura and V. Berry, *ACS Nano*, 2015, **9**, 2227–2230.

7 (*a*) A. Kozhakhmetov, S. Stolz, A. M. Z. Tan, R. Pendurthi, S. Bachu, F. Turker, N. Alem, J. Kachian, S. Das, R. G. Hennig, O. Gröning, B. Schuler and J. A. Robinson, *Adv. Funct. Mater.*, 2021, **31**, 2105252; (*b*) M. Cargnello, A. C. Johnston-Peck, B. T. Diroll, E. Wong, B. Datta, D. Damodhar, V. V. T. Doan-Nguyen, A. A. Herzing, C. R. Kagan and C. B. Murray, *Nature*, 2015, **524**, 450–453; (*c*) S. Lei, X. Wang, B. Li, J. Kang, Y. He, A. George, L. Ge, Y. Gong, P. Dong, Z. Jin, G. Brunetto, W. Chen, Z.-T. Lin, R. Baines, D. S. Galvão, J. Lou, E. Barrera, K. Banerjee, R. Vajtai and P. Ajayan, *Nat. Nanotechnol.*, 2016, **11**, 465–471; (*d*) X. Zhang, Q. Liao, S. Liu, Z. Kang, Z. Zhang, J. Du, F. Li, S. Zhang, J. Xiao, B. Liu, Y. Ou, X. Liu, L. Gu and Y. Zhang, *Nat. Commun.*, 2017, **8**, 15881; (*e*) Y. Gong, H. Yuan, C.-L. Wu, P. Tang, S.-Z. Yang, A. Yang, G. Li, B. Liu, J. van de Groep, M. L. Brongersma, M. F. Chisholm, S.-C. Zhang, W. Zhou and Y. Cui, *Nat. Nanotechnol.*, 2018, **13**, 294–299.

8 Y.-M. Chang, S.-H. Yang, C.-Y. Lin, C.-H. Chen, C.-H. Lien, W.-B. Jian, K. Ueno, Y.-W. Suen, K. Tsukagoshi and Y.-F. Lin, *Adv. Mater.*, 2018, **30**, 1706995.

9 H. Nan, Z. Wang, W. Wang, Z. Liang, Y. Lu, Q. Chen, D. He, P. Tan, F. Miao, X. Wang, J. Wang and Z. Ni, *ACS Nano*, 2014, **8**, 5738–5745.

10 (*a*) Y. Ke, X. Song, D. Qi, J. Liu, Q. Hao, Z. Wang, S. Tang and W. Zhang, *Adv. Electron. Mater.*, 2020, **6**, 2000532; (*b*) S.-Y. Seo, J. Park, K. Song, S. Cha, S. Sim, S.-Y. Choi, H. W. Yeom, H. Choi and M.-H. Jo, *Nat. Electron.*, 2018, **1**, 512–517; (*c*) X. Wang, B. Wang, Q. Zhang, Y. Sun, E. Wang, H. Luo, Y. Wu, L. Gu, H. Li and K. Liu, *Adv. Mater.*, 2021, **33**, 2102435; (*d*) C. Zhu, X. Zhao, X. Wang, J. Chen, P. Yu, S. Liu, J. Zhou, Q. Fu, Q. Zeng, Y. He, J. H. Edgar, S. J. Pennycook, F. Liu and Z. Liu, *Adv. Funct. Mater.*, 2021, **31**, 2009549; (*e*) S. Aftab, Samiya, Rabia, S. Yousuf, M. U. Khan, R. Khawar, A. Younus, M. Manzoor, M. W. Iqbal and M. Z. Iqbal, *Nanoscale*, 2020, **12**, 15687–15696.

11 J. Huo, Y. Xiao, T. Sun, G. Zou, D. Shen, B. Feng, L. Lin, W. Wang, G. Zhao and L. Liu, *ACS Appl. Mater. Interfaces*, 2021, **13**, 54246–54257.

12 (*a*) S. Wang, Z. Zhou, B. Li, C. Wang and Q. Liu, *Mater. Today Nano*, 2021, **16**, 100142; (*b*) B.-W. Su, X.-L. Zhang,

W. Xin, H.-W. Guo, Y.-Z. Zhang, Z.-B. Liu and J.-G. Tian, *J. Mater. Chem. C*, 2021, **9**, 2599–2619.
13 S. L. Fang, C. A. Y. Han, W. H. Liu, X. Li, X. L. Wang, X. D. Huang, J. Wan, S. Q. Fan, G. H. Zhang and L. Geng, *Nanotechnology*, 2021, **32**, 245102.
14 B. Wang, S. Yang, C. Wang, M. Wu, L. Huang, Q. Liu and C. Jiang, *Nanoscale*, 2017, **9**, 10733–10740.
15 (*a*) J. U. Salmón-Gamboa, A. H. Barajas-Aguilar, L. I. Ruiz-Ortega, A. M. Garay-Tapia and S. J. Jiménez-Sandoval, *Sci. Rep.*, 2018, **8**, 8093; (*b*) Y. Tan, F. Luo, M. Zhu, X. Xu, Y. Ye, B. Li, G. Wang, W. Luo, X. Zheng, N. Wu, Y. Yu, S. Qin and X.-A. Zhang, *Nanoscale*, 2018, **10**, 19964–19971; (*c*) E. Bianco, R. Rao, M. Snure, T. Back, N. R. Glavin, M. E. McConney, P. M. Ajayan and E. Ringe, *Nanoscale*, 2020, **12**, 12613–12622.
16 H. Xia, M. Luo, W. Wang, H. Wang, T. Li, Z. Wang, H. Xu, Y. Chen, Y. Zhou, F. Wang, R. Xie, P. Wang, W. Hu and W. Lu, *Light: Sci. Appl.*, 2022, **11**, 170.